NJC

Accepted Manuscript

This is an *Accepted Manuscript*, which has been through the Royal Society of Chemistry peer review process and has been accepted for publication.

Accepted Manuscripts are published online shortly after acceptance, before technical editing, formatting and proof reading. Using this free service, authors can make their results available to the community, in citable form, before we publish the edited article. We will replace this *Accepted Manuscript* with the edited and formatted *Advance Article* as soon as it is available.

You can find more information about *Accepted Manuscripts* in the Information for Authors.

Please note that technical editing may introduce minor changes to the text and/or graphics, which may alter content. The journal's standard Terms & Conditions and the Ethical guidelines still apply. In no event shall the Royal Society of Chemistry be held responsible for any errors or omissions in this *Accepted Manuscript* or any consequences arising from the use of any information it contains.

ROYAL SOCIETY OF CHEMISTRY

www.rsc.org/njc

Journal Name

RSC Publishing

ARTICLE

Highly photoactive SnO_2 nanostructures engineered by electrochemically active biofilm†

Cite this: DOI: 10.1039/x0xx00000x

Sajid Ali Ansari, Mohammad Mansoob Khan, M. Omaish Ansari, Jintae Lee and Moo Hwan Cho*

Received 00th January 2012,
Accepted 00th January 2012

DOI: 10.1039/x0xx00000x

www.rsc.org/

This paper reports the defect-induced band gap narrowing of pure SnO_2 nanostructures (*p*-SnO_2) using an electrochemically active biofilm (EAB). The proposed approach is biogenic, simple and green. Systematic characterization of the modified SnO_2 nanostructures (*m*-SnO_2) revealed EAB-mediated defects in pure SnO_2 nanostructures (*p*-SnO_2). *m*-SnO_2 nanostructures in visible light showed the enhanced photocatalytic degradation of p-nitrophenol and methylene blue compared to *p*-SnO_2 nanostructures. Photoelectrochemical studies, such as electrochemical impedance spectroscopy and linear scan voltammetry, also revealed a significant increase in the visible light response of *m*-SnO_2 compared to *p*-SnO_2 nanostructures. The enhanced activities of *m*-SnO_2 in visible light was attributed to the high separation efficiency of the photoinduced electron-hole pairs due to surface defects mediated by EAB, resulting in band gap narrowing of the *m*-SnO_2 nanostructures. The tuned band gap of the *m*-SnO_2 nanostructures enables the harvesting of visible light to exploit the properties of metal oxide towards photodegradation, which can in turn be used for environmental remediation applications.

Introduction

Organic pollutants released from industrial waste are quite toxic to humans, even at low concentrations.[1] Considerable efforts have been made to develop effective photocatalysts for the degradation of organic pollutants.[2] Among these, metal oxide nanostructures used as a photocatalyst showed the excellent degradation of organic and toxic pollutants due to their high reactivity at low concentrations, low toxicity and high stability.[3] On the other hand, in practical applications, such as photocatalytic and photoelectrochemical reactions, the use of many metal oxide nanostructures is limited by their wide band gap, which requires high energy radiation (UV) to make it photoactive.[4] The solar spectrum contains ~43% visible and only ~5% UV light.[5] Therefore, most oxide materials make use of only a small portion of the solar spectrum for traditional photocatalysis. In recent years, several methods, such as high-temperature hydrogenation,[6] electron beam irradiation,[7] metal or non-metal doping,[8] and formation of hetero structures,[9] has been used to achieve the maximum efficiency of metal oxide nanostructures to utilize visible light rather than UV light.

Metal oxide nanostructures such as TiO_2, ZnO, WO_3, Fe_2O_3 etc. have been largely studied for their photocatalytic properties since several years.[10-15] Among the many metal oxide nanostructures, SnO_2 is one of the most recognized and suitable candidate for a range of applications, such as optoelectronic devices and dye sensitized solar cells, owing to its excellent optical and electrical properties.[16] SnO_2 normally exhibits high photocatalytic activity under UV light irradiation, and considerable efforts have been made to enhance its photoactivity in the visible region.[17,4] The introduction of defects to the SnO_2 lattice appears to be a promising approach for shifting the optical absorption edge to lower energies, thereby increasing the absorption in visible region.[18-19] The defects in metal oxide nanostructures are caused mainly by the formation of low valent cations, as well as oxygen vacancies, which affects band gap narrowing significantly.[18,20-22] This opens up new possibilities for their utilization in visible light photocatalytic activities.[23-24]

A few methods for inducing defects in SnO_2 have been proposed. For example, Li et al.[19] reported the low temperature hydrothermal synthesis of SnO_2 with oxygen vacancies, whereas Kamble et al.[25] induced defects in SnO_2 using a combustion method. Ahmed et al.[26] used a sol-gel method and examined band gap narrowing in SnO_2 nanoparticles. Nevertheless, most engineering methods require harmful chemicals, and the discharge of post experimental effluents in the biosphere, which is a major concern. Therefore, a greener route for the modification of metal oxide nanostructures is needed.

Recently, electrochemically active biofilm (EABs) were reported to narrow the band gap of metal oxide (TiO_2 and ZnO) nanostructures.[20,24] In this study, an attempt was made to expand the photoresponse of pure SnO_2 nanostructures (*p*-SnO_2) in the visible region using EAB as a defect engineer. The characterization of

modified SnO_2 (*m*-SnO_2) suggests that the defects were introduced in *p*-SnO_2 upon an interaction with electrons and protons produced by the EAB, which resulted in band gap narrowing. The enhanced photocatalytic activity in the visible region shows the introduction of surface defects in SnO_2 nanostructures. *m*-SnO_2 nanostructures were employed successfully for the degradation of *p*-nitrophenol (4-NP) and methylene blue (MB) under visible light irradiation. The enhanced visible light photocatalytic activity originates from the efficient separation of photoinduced electron-hole pairs, due to defects induced by EAB in *m*-SnO_2. Furthermore, measurements of the photoelectrochemical response, such as electrochemical impedance spectroscopy (EIS) and linear scan voltammetry under dark and visible light irradiation also support the enhancement of the visible light-driven photocatalytic activities of *m*-SnO_2.

Experimental

Materials

SnO_2 nanostructure and MB were purchased from Sigma–Aldrich. Sodium acetate, sodium sulfate (Na_2SO_4) and 4-NP were obtained from Duksan Pure Chemicals Co. Ltd., South Korea and used as received. Ethyl cellulose and α-terpineol were acquired from KANTO Chemical Co., Japan and fluorine-doped transparent conducting oxide glass (FTO; F-doped SnO_2 glass; 7 Ω / sq) was supplied by Pilkington, USA. Carbon paper (without wet proof, Fuel Cell Earth LLC, USA) and all other chemicals used in this study were of analytical grade and used as received. All solutions were prepared from deionized water obtained using a PURE ROUP 30 water purification system.

Methods

X-ray diffraction (XRD, PANalytical, X'pert PRO-MPD, Netherland) was carried out using Cu Kα radiation (λ = 0.15405 nm). The XRD peaks of the crystalline phases were compared with those of the standard compounds reported in the JCPDS data file. A UV-VIS-NIR spectrophotometer (VARIAN, Cary 5000, USA) was used to record the diffuse reflectance/absorbance spectra (DRS) of the *p*-SnO_2 and *m*-SnO_2 nanostructures in the range of 200-800 nm. The photoluminescence (PL) of the *p*-SnO_2 and *m*-SnO_2 nanostructures were recorded over the range, 200-800 nm, using a Kimon, 1 K, Japan. The size of the pure SnO_2 (*p*-SnO_2) and EAB-modified SnO_2 nanostructures were observed by field emission transmission electron microscopy (FE-TEM, Tecnai G2 F20, FEI, USA) with an accelerating voltage of 200 kV combined with energy dispersive spectrometry (EDS), selected-area electron diffraction (SAED) and high angle annular dark field (HAADF). X-ray photoelectron spectroscopy (XPS, ESCALAB 250) was performed using a monochromatized Al Kα x-ray source (hν = 1486.6 eV) with a 500 μm spot size. The binding energy of C1s was used to calibrate the other binding energies. The XP spectra were fitted using the "Avantage program". The Brunauer–Emmett–Teller (BET) specific surface area of samples was measured using a Belsorp II-mini (BEL, Japan Inc.). The photoelectrochemical and photocatalytic experiments were carried out using a 400 W lamp with an intensity of 31 mW/cm^2 (3M, λ > 500 nm, USA). EIS and linear scan voltammetry (LSV) were performed in a three electrode cell with a 0.2 M Na_2SO_4 aqueous solution as the electrolyte using a potentiostat (VersaSTAT 3, Princeton Research, USA). The working electrodes were prepared according to previous reports.[20] Briefly, 100 mg of the *p*-SnO_2 and *m*-SnO_2 nanostructures were suspended thoroughly using a conditioning mix by adding ethyl cellulose as a binder and α-terpineol as a solvent for the paste, and then coated onto a FTO glass electrode using the doctor-blade method. The *p*-SnO_2 and *m*-SnO_2 nanostructure-coated (FTO) glass substrates were used as the working electrodes. Ag/AgCl (saturated with KCl) and Pt gauge were used as the reference and counter electrodes, respectively.

Electrochemically active biofilm formation

The EABs were developed on plain carbon paper according to previous reports.[27-33] Briefly, carbon paper with a size of 2.5 cm × 4.5 cm was dipped into a mineral salt medium containing sodium acetate (1 g/ L) as the substrate and carbon source in a 250 mL bottle. 10 mL of anaerobic sludge (from a biogas plant in Paju, Korea) was added under strict anaerobic conditions by sparging N_2 gas for 5 min to remove the environmental oxygen. All media, including the bacterial inoculum, were changed every two days under strict anaerobic conditions. This process was repeated for two weeks, and a living EAB formed on the surface of the carbon paper.

Modification of SnO_2 nanostructures by electrochemically-active biofilm

In typical modification process (Fig. S1), 4 mM SnO_2 nanostructures was dispersed in 200 mL of distilled water, and 0.2 g sodium acetate (1 g/L) was added as an electron donor with continuous magnetic stirring for 1 h at room temperature. Subsequently, the as-prepared EAB was hung under anaerobic conditions in a solution with slow magnetic stirring. The color of the solution turned light gray after 72 h, at which time, the solution was centrifuged to obtain the product. The as-prepared powder was then dried and isolated for further characterization.

As a control experiment, another modification process was carried out in the absence of sodium acetate, i.e. in a 4 mM solution of SnO_2, and EAB was hung under anaerobic conditions by sparging N_2 gas. The other experiment was performed by adding 0.2 g sodium acetate (1g/L) to a 4 mM SnO_2 solution in the absence of EAB under anaerobic conditions by sparging N_2 gas. In both cases, no color change was observed, even after 72 h.

Photocatalytic evaluation

The photocatalytic activities of the *p*-SnO_2 and *m*-SnO_2 nanostructures were evaluated by the degradation of 4-NP and MB under visible light irradiation. In a typical photodecomposition process, 2 mg each of *p*-SnO_2 and *m*-SnO_2 nanostructures photocatalyst were added in two different solutions, 20 mL of 4-NP

(5 mg/L) and 20 mL of MB (10 mg/L), and agitated for 30 min in the dark to achieve the adsorption-desorption equilibrium (Fig. S2 and S3). The above suspensions were irradiated with visible light. After a certain time interval (1 h), 2 mL of the solution was taken and the catalyst was separated from the solution by centrifugation to obtain a clear liquid from which the UV-Vis spectra was measured and the extent of degradation was determined. Each experiment was performed in triplicate to confirm the photocatalytic activities of the *p*-SnO_2 and *m*-SnO_2 nanostructures.
Blank reaction with catalyst (3h) in the dark (Fig. S4 and S5) and without catalyst (3h) in the light (Fig. S6 and S7) confirmed that the self-degradation of 4-NP and MB was negligible.

Photoelectrochemical studies (EIS and LSV)

To examine the photoelectrochemical response of the *p*-SnO_2 and *m*-SnO_2 nanostructures, EIS and LSV experiments were carried out under ambient conditions in the dark and under visible light irradiation in 50 mL of a 0.2 M Na_2SO_4 aqueous solution at room temperature. For each electrode, EIS was first performed in the dark and later under visible light irradiation ($\lambda > 500$ nm) at 0.0 V with frequencies ranging from 1 – 10^4 Hz. The photocurrent response was obtained by LSV under dark and visible light irradiation at a scan rate of 50 mV/s over a potential range, -0.7 to 1.0 V.

Results and discussion

Proposed modification mechanism

An EAB provides an excess of electrons and protons by decomposing the carbon source (sodium acetate) biologically.[27-33] These electrons and protons are consumed in modifying the metal oxide nanostructures.[20,24] The advantage of the EAB method is that it does not require any harmful chemicals, external energy input, capping or reducing agents, or tiresome treatments. The reaction medium for this protocol was water, and the entire modification process was carried out at 30 °C. The EAB-generated electrons and protons can interact with Sn^{4+} and surface oxygen, respectively (shown in proposed mechanism in Fig. 1). These interactions are responsible for the defect-induced band gap narrowing of the SnO_2 nanostructures, enabling visible light absorption by the *m*-SnO_2 nanostructures.

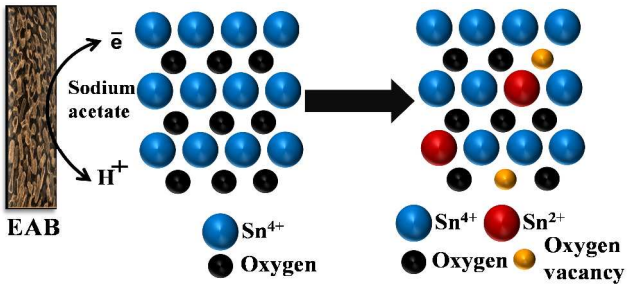

Fig. 1. Proposed mechanism for modification of the *p*-SnO_2 nanostructure by EAB.

X-ray diffraction

Fig. 2 shows XRD patterns of the *p*-SnO_2 and *m*-SnO_2 nanostructures. All the XRD peaks index corresponded to the tetragonal structure of SnO_2 (JCPDS NO. 41–1445). No peaks corresponding to any other phases were detected, confirming the high purity and single phase of the sample. The XRD peaks for the *m*-SnO_2 nanostructure appeared to be the same as that of *p*-SnO_2, except that the peak intensities were reduced slightly, possibly due to the surface modification of *p*-SnO_2. The crystallite size of *p*-SnO_2 and *m*-SnO_2 were calculated using the Scherrer equation.[20] The calculated crystallite size of *p*-SnO_2 and *m*-SnO_2 were 10.12 nm and 11.00 nm, respectively. Furthermore, a slight shift (~ 0.08) in the peak position towards a higher 2θ value was observed in the XRD pattern of the *m*-SnO_2 nanostructures (Fig. 2b). This shift can be due to the reduction of Sn^{4+} to Sn^{2+}, which leads to an increase in the number of oxygen vacancies.[34] A peak shift can also occur due to residual stress and lattice contraction (induced by defects) in the material.[20,34] Therefore, Sn^{2+} formation, residual stress and lattice contraction, appears to be responsible for the shift in the peaks.

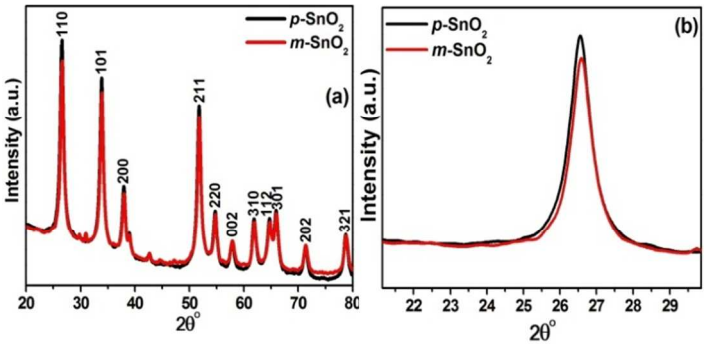

Fig. 2. (**a**) XRD patterns, and (**b**) shows the peak shift of the *p*-SnO_2 and *m*-SnO_2 nanostructures.

Optical properties

The optical properties of *p*-SnO_2 and *m*-SnO_2 nanostructures were measured by UV-vis diffuse absorption/reflectance spectroscopy in the wavelength range, 200–800 nm, and are shown in Fig. 3 and S8. The *p*-SnO_2 nanostructures showed almost no absorption in the visible region due to the large band-gap. In contrast, the *m*-SnO_2 nanostructure showed visible light absorption, which was attributed to the defects and oxygen vacancies.[7,20,23-24] The absorption edge of *m*-SnO_2 is located in the visible light region, making it an effective photocatalyst workable in visible light. From Fig. 3 one also can see that there is a red shifting of the absorption from *p*-SnO_2 (370 nm) to *m*-SnO_2 (434 nm) nanostructures. The band gap of the *p*-SnO_2 and *m*-SnO_2 nanostructures was estimated directly from the spectrum, and found to be ~ 2.85 eV for the *m*-SnO_2 nanostructures, which was red shifted compared to the *p*-SnO_2 nanostructures (E_g = 3.35 eV).[7,24] The observed band gap of the *m*-SnO_2 nanostructures was substantially smaller than that of the *p*-SnO_2 nanostructures and was attributed to the presence of defects in SnO_2.[35] On the other hand, the band gap narrowing due to oxygen vacancies and defects was also apparent from an optical absorption

study, which is further evidenced from the change in color of the powders (Fig. 3).

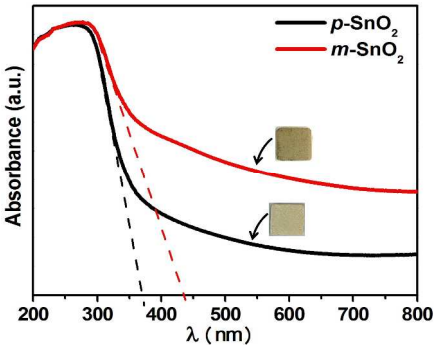

Fig. 3. UV-vis diffuse absorption spectra of the *p*-SnO_2 and *m*-SnO_2 nanostructures and direct band gap measurements.

XPS analysis

The surface chemical composition and purity of the *p*-SnO_2 and *m*-SnO_2 nanostructures were determined by XPS. The XPS survey spectra of the *p*-SnO_2 and *m*-SnO_2 revealed peaks for Sn, O and C only, but no extra peaks for other impurities, as shown in Fig. S9. Fig. 4a shows the high resolution XP spectra of Sn 3d and the binding energies at 494.94 eV and 486.52 eV corresponds to Sn $3d_{3/2}$ and Sn $3d_{5/2}$, respectively, and the valency of Sn in the SnO_2 nanostructure is Sn^{4+}. The XP spectrum of the *m*-SnO_2 nanostructures shows peaks of Sn $3d_{3/2}$ and Sn $3d_{5/2}$ shifted towards slightly lower values compared to the *p*-SnO_2 nanostructures. The corresponding binding energy of the *m*-SnO_2 nanostructure decreased to 494.64 and 486.16 eV. The difference in binding energy indicates that the electronic interactions of Sn ions are different in the *p*-SnO_2 and *m*-SnO_2 samples after an interaction with the electrons produced by EAB. According to Larciprete et al.[36], Themlin et al.[37] and Szuber et al.[38], the energy distance between the Sn^{4+} and Sn^{2+} components is equal to 0.7 eV, whereas the energy distance between the Sn^{4+} and Sn^{0} components is 2.2 eV. Therefore, from the above discussion, a shift of the Sn 3d peak towards a lower binding energy in the *m*-SnO_2 nanostructure might be due to an increase in the amount of Sn^{2+}.[39]

To analyze the oxygen vacancies in the *p*-SnO_2 and *m*-SnO_2 nanostructures, the O1s photoemission peak was deconvoluted into distinct peaks, as shown in Fig. 4b. The low binding energy peak at ~530.4 eV is normally attributed to lattice oxygen, whereas the high binding energy peak at 531.3–532.8 eV is assigned to oxygen vacancies, surface-adsorbed oxygen and hydroxyl groups.[40] The intense peak with a binding energy at ~ 530.4 eV corresponds to the Sn–O bonds, and the less intense peak at ~ 531.5 eV corresponds to oxygen vacancies. In the *m*-SnO_2 nanostructure, the peak at ~ 531.5 eV corresponding to O1s appeared more intense than that of the *p*-SnO_2 nanostructure. The intensity of the O1s peak is basically associated with variations in the concentration of oxygen vacancies. The peak at ~ 532.7 eV indicates the formation of hydroxyl groups on the *m*-SnO_2 surface, which might be due to an interaction of protons produced by the EAB. These results show that the vacancies and defect concentration increases dramatically in the *m*-SnO_2 nanostructure after an interaction of electron and protons produced by EAB.[41]

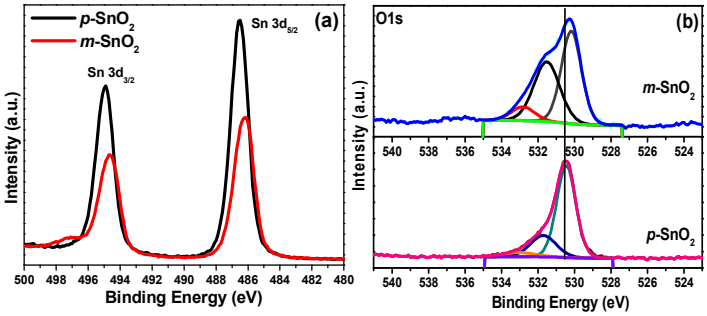

Fig. 4. XP spectra of (**a**) Sn 3d, and (**b**) O 1s spectra of the *p*-SnO_2 and *m*-SnO_2 nanostructures.

TEM analysis

Fig. 5 presents the TEM and HR-TEM images of SnO_2 nanostructures (*p*-SnO_2 and *m*-SnO_2). Fig. 3a and 3a' show the spherical shape of the *p*-SnO_2 and *m*-SnO_2 nanostructures, which are in the range of ~20 nm in diameter. The SAED patterns shown in the Fig. S10 and S11 confirms the single crystalline nature of the SnO_2 nanostructures. The HR-TEM image in Fig. 3c and 3c' show lattice fringes with a spacing of 0.33 nm, which is in good agreement with the spacing of the (1 1 0) planes of SnO_2. The structural compositions of the particles were determined by HAADF-FETEM, and are shown in Fig. S12 and S13 for *p*-SnO_2 and *m*-SnO_2, respectively. The EDX spectra in Fig. S14 and S15 showed that only Sn and O were present in the sample, confirming the absence of the other impurities. These results are consistent with the XRD data.

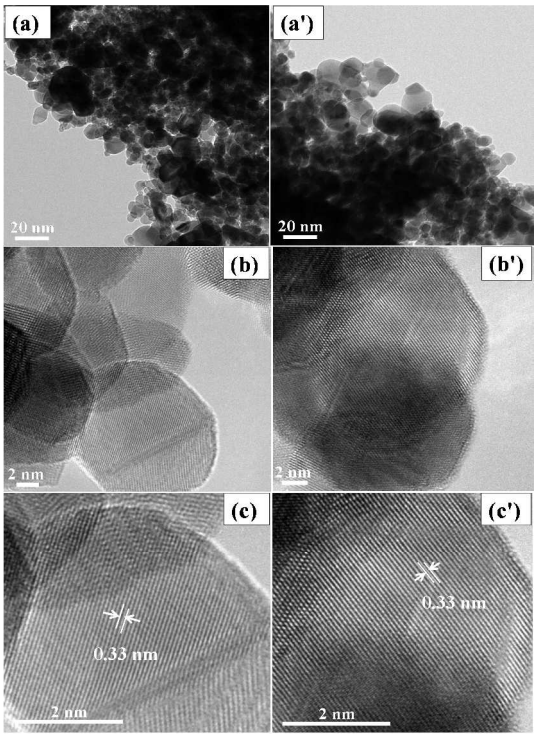

Fig. 5. TEM and HR-TEM images of the *p*-SnO_2 and *m*-SnO_2 nanostructures.

PL analysis

The emission characteristics of the *p*-SnO_2 and *m*-SnO_2 nanostructures were examined by PL spectroscopy at room temperature, and are shown in Fig. 6. The PL spectra showed a very strong emission peak at ~ 600 nm.[42] The excitonic PL intensities of *p*-SnO_2 were greater than those of the *m*-SnO_2 nanostructures, indicating the recombination of electrons and holes occurring quite easily in the case of the *p*-SnO_2 nanostructures. On the other hand, the defect emission band decreased significantly in the case of the *m*-SnO_2 nanostructures and was related to the increase in defects and oxygen vacancies.[43] This suggests that the *m*-SnO_2 nanostructures improves the separation of photo-induced electrons and holes, and suppresses the automatic recombination process of photogenerated electrons and holes.[20] In general, weaker the excitonic PL intensity, higher the separation rate of photo-induced charge carriers.[44] The results also indicate the substantial quenching of PL by the defects present in *p*-SnO_2. This helps promote the separation rates of photogenerated electrons and holes, thereby favoring the photocatalytic activity.

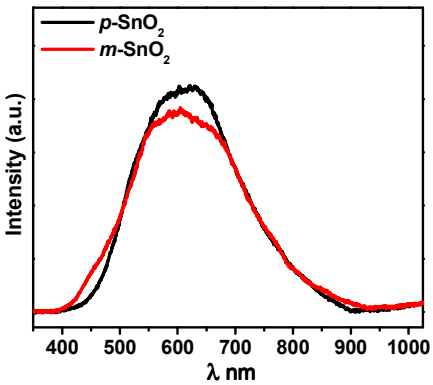

Fig. 6. PL spectra of the *p*-SnO_2 and *m*-SnO_2 nanostructures.

Visible light photocatalytic performance of the *p*-SnO_2 and *m*-SnO_2 nanostructures

To examine the influence of defects on the photocatalytic efficiency of *m*-SnO_2 nanostructures, the photocatalytic experiments were carried out under visible light irradiation for the degradation of colorless aromatic compounds (4-NP) and colored dye (MB) in water. The decreasing intensity of the absorption of 4-NP and MB were used to determine the photocatalytic activity of the *m*-SnO_2 nanostructures, corresponding to photodegradation of the dye. Fig. 7a and 7b shows plots of the degradation (C/C_0) versus irradiation time, where C is the absorption of a 4-NP and MB solution at each time interval of irradiation, and C_0 is the absorption of the initial concentration (time 0). After irradiation for 5 h and 6 h, approximately 80% of the 4-NP and 85% of MB had degraded, respectively. Furthermore, the photocatalytic degradation kinetics of 4-NP and MB were investigated and results are shown in Fig S16. The changes of the 4-NP and MB concentration versus the reaction time over the pure and modified SnO_2 followed pseudo-first-order kinetics plot by the equation reported elsewhere.[8-9,45] These results reveal that the *m*-SnO_2 shows higher rate constants than *p*-SnO_2 nanostructures. The pseudo-first-order constants for 4-NP and MB are summarized in Table S1. The *m*-SnO_2 showed ~3 and 4.5 times higher visible light degradation than the *p*-SnO_2 for 4-NP and MB, respectively. The *m*-SnO_2 shows highest photocatalytic performance and fully photodegrade the organic pollutants, although it had very low surface area (21.10 m^2/g) as compared to *p*-SnO_2 (36.73 m^2/g).[46] The observed high photocatalytic activity of *m*-SnO_2 is believed because of various defects, high absorbance (Fig. 3) and low PL intensity (Fig. 6).

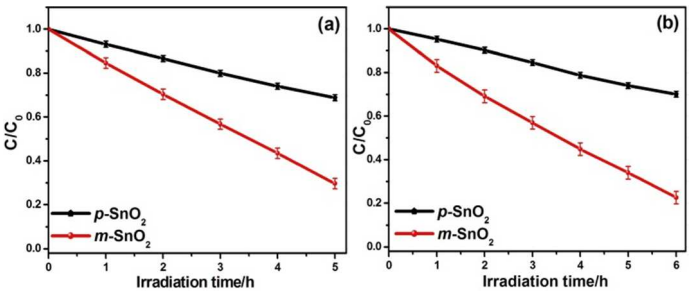

Fig. 7. C/C_0 versus irradiation time (h) plot for the photodegradation of (**a**) 4-NP (**b**) MB by *p*-SnO_2 and *m*-SnO_2 nanostructures under visible light irradiation.

The enhancement in photocatalysis after modification of the *p*-SnO_2 nanostructures was attributed to the effective separation of electron-hole pairs at the *m*-SnO_2 surfaces. Compared to *p*-SnO_2 nanostructures, the *m*-SnO_2 nanostructures exhibited higher absorbance (Fig. 3) in the visible range, resulting in an increase in the number of photo-generated electrons and holes that participate in the photocatalytic reaction, which was confirmed by DRS. The above results shows that the *p*-SnO_2 nanostructure is a poor photocatalyst and shows very weak photodegradation ability. This can be attributed to the adsorption of dyes on the surface of *p*-SnO_2 and it is evident by the dark reaction with catalyst (Fig. S4 and S5), whereas the *m*-SnO_2 nanostructures shows enhanced photodegradation, which is achieved by the defects in *m*-SnO_2 induced by EAB. The efficient charge separation in the *m*-SnO_2 nanostructures revealed the presence of defects, which is also consistent with the other characterization results. The resulting band gaps of *p*-SnO_2 and *m*-SnO_2 nanostructures measured directly from the spectra (Fig. 3) show that the band gap of the *m*-SnO_2 nanostructure is apparently smaller than that of the *p*-SnO_2 nanostructure. The difference in band gap between the two samples is attributed to the high percentage of oxygen vacancies and other defects in the *m*-SnO_2 nanostructure.[20] When the *m*-SnO_2 nanostructures are illuminated by visible light (Fig. 8) greater than the band gap energy, electrons are promoted from the valence band to the conduction band, leaving behind holes in the valence band. These photoelectrons can react with the surface-adsorbed O_2 to form

superoxide radical anions and photoinduced holes. The latter reacts with surface-adsorbed hydroxyl ions to form highly reactive hydroxyl radicals. These hydroxyl radicals are mainly responsible for the degradation of 4-NP and MB through a series of chemical reactions, as shown in Fig. 8. Following are the reactions that occurred for the degradation of pollutants.

$$m\text{-}SnO_2 + h\nu \text{ (visible light)} \rightarrow e^- + h^+$$
$$e^- + O_2 \rightarrow O_2^{\bullet -}$$
$$h^+ + OH^- \rightarrow {}^{\bullet}OH$$
$$O_2^{\bullet -} + H_2O \rightarrow {}^{\bullet}OH$$
$${}^{\bullet}OH + \text{Pollutants} \rightarrow \text{Degradation of pollutants}$$

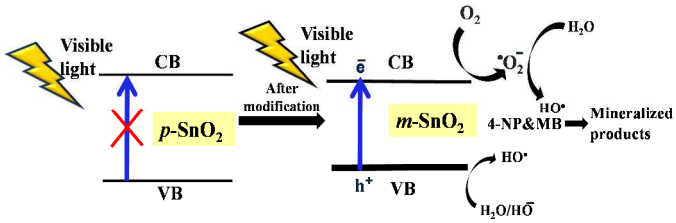

Fig. 8. Proposed mechanism for the photodegradation of 4-NP and MB by the *m*-SnO_2 nanostructures.

Stability and reusability of the *m*-SnO_2

The reusability of *m*-SnO_2 was tested by centrifuging the catalyst from the dye solution, later washing with DI water and drying in an air oven at 100 ^{o}C. The reused catalyst showed a similar response to that of the fresh catalyst, highlighting the stability of *m*-SnO_2 nanostructures.

Photoelectrochemical Study

EIS was used to examine the charge separation efficiency of *p*-SnO_2 and *m*-SnO_2 nanostructures under dark and visible light irradiation (Fig. 9a). The semicircle in the Nyquist plot is the expected response of the simple circuit. EIS Nyquist plots are also employed to examine the charge transfer resistance and separation efficiency between the photogenerated electrons and holes.[47-48] The shape of the semicircular arcs in the EIS spectra is a manifestation of the magnitude of charge transfer resistance (R_{ct}) and constant phase element (CPE) at the photocatalyst/electrolyte interface.[4] Upon irradiation with visible light, the arc radius in the case of *m*-SnO_2 becomes smaller than *p*-SnO_2 due to the increased electronic conductivity of the electrodes. In other words, the smaller the arc radius, smaller the charge transfer resistance and the higher the efficiency of charge separation, leading to the higher photocatalytic activity of *m*-SnO_2.[49-50] These results suggest that *m*-SnO_2 has a lower resistance to interfacial charge transfer and effective separation of photogenerated electron hole pairs than that of *p*-SnO_2.[20] The significant enhancement in photocatalytic activity is due mainly to an increase in the amount of different types of defects. EIS showed that *m*-SnO_2 imparts lower charge transfer resistance and might exhibit higher photocatalytic activity for dye degradation under visible light irradiation.

Fig. 9b shows linear scan voltammograms of the *p*-SnO_2 and *m*-SnO_2 nanostructures in the dark and under visible light irradiation, respectively, in which the photocurrent shown by the *m*-SnO_2 nanostructures under visible light irradiation appears to be enhanced greatly compared to the *p*-SnO_2 nanostructures. The improved the photocurrent response of *m*-SnO_2 was attributed to the increase in light absorption ability due to band gap narrowing. Defects, such as oxygen vacancies, play an important role in narrowing the band gap.[20] Owing to the sufficiently narrow band gap of SnO_2, the valence electrons of SnO_2 can be excited to the conduction band state by absorbing visible light. The photoelectrochemical activity is determined by both the light-harvesting capacity and the separation of electron–hole pairs. A high photocurrent normally indicates the efficient generation and transfer of the photoexcited charge carriers under visible light irradiation.[22] Such enhanced photoelectrochemical performance of *m*-SnO_2 is due to the increased oxygen vacancies in the lattice that provide efficient transport pathways for electrons. The photocurrent densities are closely related to the generation of photoelectrons, and the defects enhance the transfer of photoelectrons.[21] The *m*-SnO_2 has a higher photocurrent than *p*-SnO_2 under similar conditions, suggesting that *m*-SnO_2 exhibits greater efficiency of the separation of electron-hole pairs compared to *p*-SnO_2. In addition, EIS (under visible light) and PL showed that the charge separation efficiency of *m*-SnO_2 is also much higher than *p*-SnO_2, and the *m*-SnO_2 shows high visible photocatalytic activity. The results suggest that the disorder or defect in nanostructures can effectively suppress the recombination of photogenerated electron–hole pairs and promote the photoelectric activity of *m*-SnO_2 nanostructures.

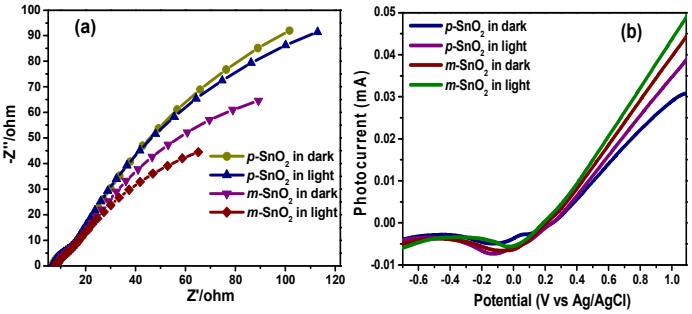

Fig. 9. (a) Nyquist plots, and **(b)** Linear scan voltammograms of *p*-SnO_2 and *m*-SnO_2 nanostructures photoelectrodes under dark and visible light irradiation.

Conclusions

A green and an efficient biogenic method was proposed using EAB for the band gap narrowing of *p*-SnO_2 nanostructures by creating surface defects. UV-Vis-NIR absorption spectroscopy revealed a reduced band gap of the *m*-SnO_2 nanostructures due to the presence of vacancies and defects. The formation of vacancies and defects was examined using a range of characterization techniques,, and results were well correlated with the mechanism proposed to explain the visible light activity. Compared to *p*-SnO_2, the *m*-SnO_2

showed significantly higher photocatalytic activity towards 4-NP and MB degradation under visible light irradiation than *p*-SnO_2. The decrease in the band gap of the *m*-SnO_2 nanostructures induced by vacancies and defects was the main reason for the enhanced visible light photocatalytic and photoelectrochemical activities. Surface defects, such as oxygen vacancies, can facilitate the separation of photoexcited electron–hole pairs, and increase the photocatalytic and photoelectrochemical performance, such as EIS and LSV. PL provided conclusive evidence of the enhanced visible light activity of *m*-SnO_2 nanostructures. The proposed green and effective approach is an edge over UV light photocatalysis. The new method is a paradigm shift in the development of new photocatalyst materials, and can be extended to a wider range of materials incorporating band gap engineering.

Acknowledgements

This study was supported by Basic Science Research Program through the National Research Foundation of Korea (NRF) funded by the Ministry of Education, Science and Technology (Grant No: 2012R1A1A4A01005951).

Notes and references

School of Chemical Engineering, Yeungnam University, Gyeongsan-si, Gyeongbuk 712-749, South Korea. Phone: +82-53-810-2517; Fax: +82-53-810-4631,
***Email:** mhcho@ynu.ac.kr*

†Electronic Supplementary Information (ESI) available: [schematic representation of modification process, SEAD patterns, HAADF FE-TEM images, images, EDX, DRS spectra, XPS survey spectra of *p*-SnO_2 and *m*-SnO_2 nanostructures, Kinetic fit spectra and rate constant table of 4-NP and MB degradation, adsorption-desorption equilibrium spectra, dark reaction (with catalyst) spectra, light reaction (without catalyst) spectra of 4-NP and MB] See DOI: 10.1039/b000000x/

1 Z. F. Tian, C. H. Liang, J. Liu, H. M. Zhang and L. D. Zhang, *J. Mater. Chem.*, 2011, **21**, 18242−18247.
2 L. Jing, W. Zhou, G. Tian and H. Fu, *Chem. Soc. Rev.*, 2013, **42**, 9509−9549.
3 Y. Wang, Q. Wang, X. Zhan, F. Wang, M. Safdar and J. He, *Nanoscale*, 2013, **5**, 8326−8339.
4 X. Liu, L. Pan, T. Chen, J. Li, K. Yu, Z. Sun, C. Sun, *Catal. Sci. Technol.*, 2013, **3**, 1805−1809.
5 T. Pal, A. K. Sinha, P. K. Manna, M. Pradhan, C. Mondal and S. M. Yusuf, *RSC Adv.*, 2013, **4**, 208−211.
6 X. Chen, L. Liu, P. Y. Yu and S. S. Mao, *Science*, 2011, **331**, 746−750.
7 M. M. Khan, S. A. Ansari, D. Pradhan, M. O. Ansari, D. H. Han, J. Lee and M. H. Cho, J. *Mater. Chem. A*, 2014, **2**, 637−644.
8 L. Li, Y. Zhang, A. M. Schultz, X. Liu, P. A. Salvador and G. S. Rohrer, *Catal. Sci. Technol.*, 2012, **2**, 1945–1952.
9 L. Li, X. Liu, Y. Zhang, N. T. Nuhfer, K. Barmak, P. A. Salvador and G. S. Rohrer, *ACS Appl. Mater. Interfaces,* 2013, **5**, 5064−5071.
10 Y. Liu, L. Yu, Y. Hu, C. Guo, F. Zhangand, X. W. (David) Lou, *Nanoscale*, 2012, **4**, 183–187.
11 C. Wen, F. Liao, S. Liu, Y. Zhao, Z. Kang, X. Zhang and M. Shao, *Chem. Commun.*, 2013, **49**, 3049–3051.
12 F. Wang, C. D. Valentin and G. Pacchioni, *ChemCatChem*, 2012, **4**, 476–478.
13 W.-J. Ong, M. M. Gui, S.-P. Chai and A. R. Mohamed, *RSC Adv.*, 2013, **3**, 4505–4509.
14 C. Feng, S. Wang and B. Geng, *Nanoscale*, 2011, **3**, 3695–3699.
15 W.-J. Ong, L.-L. Tan, S.-P. Chai, S.-T. Yong and A. R. Mohamed, *Nanoscale*, 2014, DOI: 10.1039/C3NR04655A.
16 Asdim, K. Manseki, T. Sugiura and T. Yoshida, *New J. Chem.*, 2014, DOI: 10.1039/C3NJ01278F.
17 B. Jia, W. Jia, F. Qu and X. Wu, *RSC Adv.*, 2013, **3**, 12140−12148.
18 V. B. Kamble and A. M. Umarji, *AIP ADVANCES*, 2013, **3**, 082120−082125.
19 N. Li, K. Du, G. Liu, Y. Xie, G. Zhou, J. Zhu, F. Li and H. M. Cheng, *J. Mater. Chem. A*, 2013, **1**, 1536−1539.
20 S. A. Ansari, M. M. Khan, S. Kalathil, A. Nisar, J. Lee and M. H. Cho, *Nanoscale*, 2013, **5**, 9238−9246.
21 D. F. Cox, T. B. Fryberger, and S. Semancik, *Phys. Rev. B: Condens. Matter*, 1988, **38**, 2072−2085.
22 C. M. Fan, Y. Peng, Q. Zhu, L. Lin, R. X. Wang, and A. W. Xu, *J. Phys. Chem. C*, 2013, **117**, 24157–24166.
23 J. Wang, Z. Wang, B. Huang, Y. Ma, Y. Liu, X. Qin, X. Zhang and Y. Dai, *ACS Appl. Mater. Interfaces,* 2012, **4**, 4024−4030.
24 S. Kalathil, M. M. Khan, S. A. Ansari, J. Lee and M. H. Cho, *Nanoscale*, 2013, **5**, 6323−6326.
25 V. B. Kamble, S. V. Bhat and A. M. Umarji, *J. Appl. Phys.*, 2013, **113**, 244307−244314.
26 A. S. Ahmed, S. M. Muhamed, M. L. Singla, S. Tabassum, A. H. Naqvi, and A. Azam, *J. Lumin.*, 2011, **131**, 1−6.
27 M. M. Khan, S. Kalathil, J. Lee and M. H. Cho, *Bull. Korean Chem. Soc.*, 2012, **33**, 2592–2596.
28 S. Kalathil, M. M. Khan, J. Lee and M. H. Cho, *Biotechnol. Adv.*, 2013, **31**, 915–924.
29 M. M. Khan, S. A. Ansari, J. H. Lee, J. Lee and M. H. Cho, *ACS Sustainable Chem. Eng.* 2013, DOI: 10.1021/sc400330r.
30 M. M. Khan, J. Lee and M. H. Cho, *Int. J. Hydrogen Energy*, 2013, **38**, 5243–5250.
31 M. M. Khan, S. A. Ansari, J. Lee and M. H. Cho, *Nanoscale*, 2013, **5**, 4427–4435.
32 M. M. Khan, S. A. Ansari, J. Lee and M. H. Cho, *Mater. Sci. Eng. C*, 2013, **33**, 4692–4699.
33 T. H. Han, M. M. Khan, S. Kalathil, J. Lee, M. H. Cho, *Ind. Eng. Chem. Res.*, 2013, **52**, 8174−8181.
34 B. D. Cullity and S. R. Stock in "Elements of X-ray diffraction", 3rd Edit., Prentice Hall, 2001, Chapter **4**, 123−157.
35 R. N. Mariammal, K. Ramachandran, B. Renganathan and D. Sastikumar, *Sens. Actuators., B*, 2012, **169**, 199−207.
36 R. Larciprete, E. Borsella, P. D. Padova, P. Perfetti, G. Faglia and G. Sberveglieri, *Thin Solid Films*, 1998, **323**, 291−295.
37 J. M. Themlin, M. Chtaib, L. Henrard, P. Lambin, J. Darville and J. M. Gilles, *Phys. Rev. B*, 1992, **46**, 2460−2468.

38 J. Szuber, G. Czempik, R. Larciprete and B. Adamowicz, *Sens. Actuators., B*, 2000, **70**, 177.
39 Z. F. Tian, C. H. Liang, J. Liu, H. M. Zhang and L. D. Zhang, *J. Mater. Chem.*, 2011, **21**, 18242−18247.
40 A. Galtayries, R. Sporken, J. Riga, G. Blanchard and R. Caudano, *J. Electron. Spectrosc. Relat. Phenom.*, 1998, **88**, 951−956.
41 L. T. Murciano, A. Gilbank, B. Puertolas, T. Garcia, B. Solsona and D. Chadwick, *Applied Catalysis B: Environmental*, 2013, **132–133**, 116−122.
42 J.Q. Hu, Y. Bando, Q.L. Liu and D. Golberg, *Adv. Funct. Mater.*, 2003, **13**, 493–496.
43 P. Chetri and A. Choudhury, *Physica E*, 2013, **47**, 257−263.
44 J. Liqiang, Q. Yichun, W. Baiqi, L. Shudan, J. Baojiang, Y. Libin, F. Wei, F. Honggang and S. Jiazhong, *Sol. Energy Mater. Sol. Cells*, 2006, **90**, 1773−1787.
45 M. M. Khan, S. Kalathil, J. Lee and M.H. Cho, *Bull. Korean Chem. Soc.*, 2012, **33**, 1753–1758.
46 Z. Sun, Z. Zhao, H. Tan, H. Zhao, Y. Lv, L. Zhou and Y. Song, *Chem. Commun.*, 2014, DOI: 10.1039/C3CC49182J.
47 S. A. Ansari, M. M. Khan, J. Lee and M. H. Cho, *J. Ind. Eng. Chem.* 2013, http://dx.doi.org/10.1016/j.jiec.2013.08.006.
48 X. Bai, L. Wang, R. Zong, Y. Lv, Y. Sun and Y. Zhu, *Langmuir*, 2013, **29**, 3097−3105.
49 Y. Lv, Y. Zhu, and Y. Zhu, *J. Phys. Chem. C*, 2013, **117**, 18520−18528.
50 S. A. Ansari, M. M. Khan, M. Omaish, J. Lee and M. H. Cho, *J. Phys. Chem. C* 2013, **117**, 27023−27030.